energy&fuels

pubs.acs.org/EF

Article

Soot-Free Low-NO_x Aeronautical Combustor Concept: The Lean Azimuthal Flame for Kerosene Sprays

Pedro M. de Oliveira,* Daniel Fredrich, Gianluigi De Falco, Ingrid El Helou, Andrea D'Anna, Andrea Giusti, and Epaminondas Mastorakos

Cite This: *Energy Fuels* 2021, 35, 7092−7106

Read Online

ACCESS | Metrics & More | Article Recommendations

ABSTRACT: An ultralow emission combustor concept based on "flameless oxidation" is demonstrated in this paper for aviation kerosene. Measurements of gas emissions, as well as of the size and number of nanoparticles via scanning mobility particle sizing, are carried out at the combustor outlet, revealing simultaneously soot-free and single-digit NO_x levels for operation at atmospheric conditions. Such performance, achieved with direct spray injection of the fuel without any external preheating or prevaporization, is attributed to the unique mixing configuration of the combustor. The combustor consists of azimuthally arranged fuel sprays at the upstream boundary and reverse-flow air jets injected from downstream. This creates locally sequential combustion, good mixing with hot products, and a strong whirling motion that increases residence time and homogenizes the mixture. Under ideal conditions, a clean, bright-blue kerosene flame is observed, free of soot luminescence. Although soot is intermittently formed during operation around optimal conditions, high-speed imaging of the soot luminescence shows that particles are subjected to long residence times at O_2-rich conditions and high temperatures, which likely promotes their oxidation. As a result, only nanoparticles in the 2−10 nm range are measured at the outlet under all tested conditions. The NO_x emissions and completeness of the combustion are strongly affected by the splitting of the air flow. Numerical simulations confirm the trend observed in the experiment and provide more insight into the mixing and air dilution.

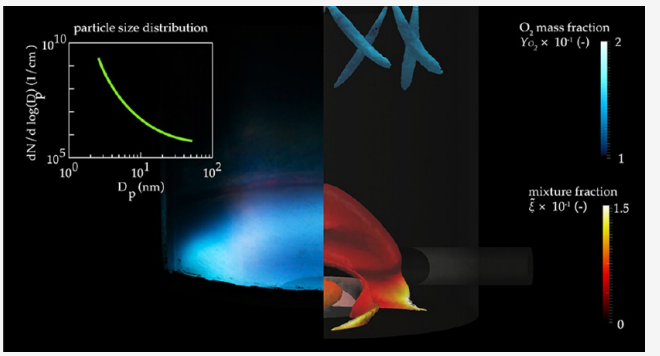

INTRODUCTION

The reduction of NO_x, CO, and particulate matter produced in the aviation sector has attracted regulatory, industrial, and societal attention as a result of the associated adverse health effects of such emissions. It has long been recognized by combustion scientists and technologists that combustor design has many competing requirements: reducing pollutants, satisfying operability (limited by ignition/relight, combustion-induced oscillations, and blow off), achieving complete combustion, achieving good mixing while paying a small pressure loss penalty, reaching the maximum possible temperature for high thermodynamic efficiency and CO burnout while keeping NO_x emissions bound, low-cost manufacturing, long life, and others.[1−4] Over the years, industry has converged to the rich−quench−lean concept (RQL, also known as "rich burn") and the lean−prevaporized−premixed concept (LPP, also known as "lean burn") as those with the highest potential to meet the above requirements.[1] While it may be possible to meet upcoming emission targets by fine tuning of such concepts, further reductions in emissions for future carbon-neutral flight require completely new combustor concepts.

The present work explores a new concept of combustor based on "flameless oxidation", a regime obtained by mixing hot products with oxidizer prior to reaction with fuel, creating a spread-out flame characterized by high reactant temperatures and low flame chemiluminescence.[5] Flameless oxidation is a promising low-NO_x, low-soot, low-CO, and low-noise technology that has been originally developed in the context of industrial furnaces.[6] Such characteristics are very attractive for the aviation sector[7] as well as the power generation sector.[2] Recently, a new combustor concept based on "flameless oxidation" was developed by the University of Cambridge,[8,9] denoted as the "lean azimuthal flame" (LEAF). Tests using CH_4 as fuel showed single-digit parts per million levels of NO, CO, and unburnt hydrocarbons, lower than those of a lean premixed flame. In the LEAF, flameless oxidation occurs as a

Special Issue: In Memory of Mario Costa

Received: November 16, 2020
Revised: January 31, 2021
Published: February 17, 2021

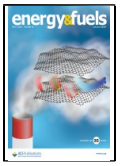

https://dx.doi.org/10.1021/acs.energyfuels.0c03860
Energy Fuels 2021, 35, 7092−7106

result of high-speed air jets injected against the net flow and fuel injection, causing entrainment of combustion products and promoting turbulence and mixing before reaction occurs. The resulting high-temperature reactants favor autoignition over flame propagation, generating a toroidal-like reaction zone.[8] In the present work, the LEAF combustor concept is advanced for kerosene spray operation, demonstrating the viability of such a low-emission concept as a liquid-fueled gas turbine combustor technology for aviation.

Although flameless oxidation of gaseous fuels has been widely studied,[5] including applications to gas turbines,[7] very few works have been carried out with liquid-fueled operation, even at the fundamental level.[10] By injection of liquid fuel directly into the combustion chamber as a spray, evaporation adds a layer of complexity to flameless oxidation by affecting how fuel is released and mixed. In addition to the thermophysical properties of the fuel, the process is strongly affected by the spray polydispersity. Large slowly evaporating droplets have been observed to penetrate across the axial length of a flameless oxidation combustor, past the main reaction zone, resulting in highly sooting and elongated flames.[11,12] To allow for flameless operation with liquid-fueled injection, experiments found that combustion product recirculation and reactant dilution ratio must be maximized by both increasing flow rates[13−15] and optmizing the orientation of multiple air jets.[16,17] This way, high mixing and dilution of freshly injected reactants was verified, leading to CO and NO_x emission levels between 1 and 10 ppm.

Furthermore, despite the achievements of the above-mentioned experimental works toward the development of liquid-fueled flameless oxidation combustors, there is a recognized lack of both numerical and experimental studies of this process that combine gaseous and particle pollutant emission measurements with observations of reaction zone structures.[7] In fact, detailed size information on nanoparticles produced during flameless oxidation and in turbulent flames in general is very limited. Scanning mobility particle sizing (SMPS) is an *ex situ* technique widely used in combustion research for that purpose, because it provides rapid, direct, and in-line measurements of particle size distributions (PSDs) in the range of 1−100 nm.[18−20] With this technique, a wide range of sooting laminar premixed and diffusion flames was characterized, adding to our understanding of soot morphology and chemistry.[20−24] In contrast, few studies applied scanning mobility particle sizing to turbulent flames, while no measurements have yet been carried out under flameless oxidation conditions. Probe sampling of flame-produced nanoparticles at the exhaust of jet flames demonstrated that monomodal PSDs are characteristic of turbulent conditions,[25,26] in contrast to the typical bimodal PSDs observed in laminar flames.[27,28] To suppress soot formation in non-premixed systems, dilution air jets are typically used (e.g., RQL combustors). The combination of SMPS probe-sampling measurements and laser-induced incandescence visualization (LII)[29] showed that dilution air jets are highly effective in oxidizing soot, leading to an overall reduction of the total particle number and soot volume fraction at the exhaust of the combustor as well as a reduction of the mean particle size. Flames that are typically not visibly sooty (observed both through natural soot luminescence or laser-induced incandescence) are, in fact, characterized by a large number of small 1−10 nm nanoparticles as a result of dilution jets.[29] Therefore, it is of paramount importance to characterize the particulate emissions over a wide range of sizes to complement visualizations of the flame. Numerical simulations could further assist the interpretation of the measurements by relating the experimental findings to the flow field structure and mixing.[30]

In this paper, we provide insight on the key physical phenomena involved in the LEAF operarting with kerosene spray injection based on a combined experimental and modeling study. The objectives are: (1) to demonstrate the LEAF operation in the context of spray combustion of real aviation fuels, (2) to evaluate the flame behavior and emission performance for a range of operating conditions, and (3) to relate the combustor performance to the flow field and mixing characteristics.

For that, a characterization of the flame behavior and resulting gas and particulate emission levels is carried out by changing the flow rates of the fuel and air streams entering the combustor. Numerical simulations based on the Eulerian−Lagrangian approach provide additional information on the complex reaction zone and extend the experimental findings to real engine conditions. The flow field, mixing of the various air streams, spray, and liquid fuel location are analyzed in detail to provide an overview of the key elements of the LEAF operation and, at the same time, provide guidelines for future development.

The paper is structured as follows: First, the experimental apparatus used to demonstrate the LEAF concept for spray combustion applications is described, followed by the experimental and numerical methods. Then, results are presented with a focus on flame visualization, emission measurements, and analysis of the mixing characteristics. Summary and conclusions close the paper.

LEAF COMBUSTOR

A summary of the main features of the LEAF combustor is given in Figure 1. The combustor is described in detail for gaseous operation by El Helou et al.;[8] in this work,

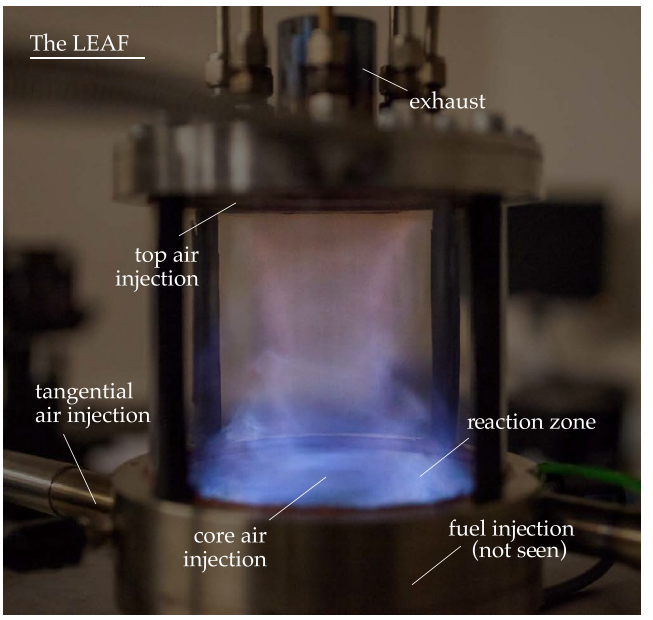

Figure 1. Overview of the liquid-fueled LEAF combustor. Stable operation of the combustor was achieved using non-prevaporized, spray-injected kerosene.

https://dx.doi.org/10.1021/acs.energyfuels.0c03860
Energy Fuels 2021, 35, 7092−7106

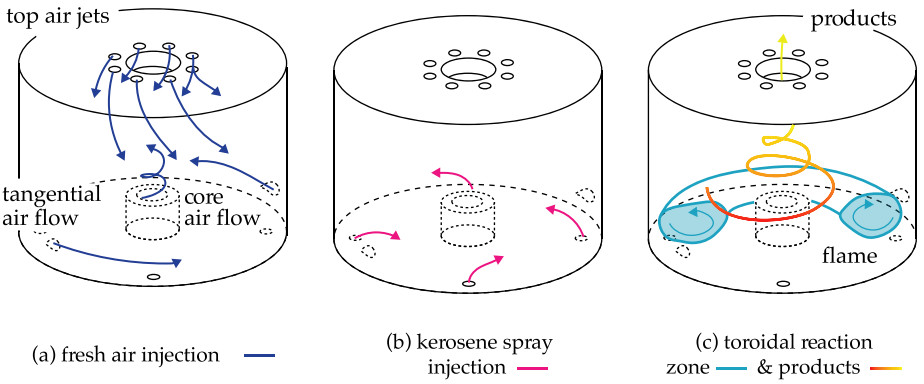

Figure 2. Illustration of the liquid-fueled LEAF combustor.

modifications have been made to allow for liquid fuel operation. The combustor consists of a cylindrical combustion chamber in quartz, where air is injected from multiple angled orifices at the top, shown schematically in Figure 2. This reverse-flow injection induces a whirling motion around the central axis of the combustor and generates high turbulence (Figure 2a). Additionally, air is injected from two tangential ports, which are also used as pilots to ignite the kerosene flame by simply injecting a premixed air−methane mixture and stabilizing a small flame at the bluff bodies located flush to the wall. A third port for air injection, which will be referred to as "core" flow, is placed at the bottom plate, at the center axis of the burner. The core flow is introduced in the chamber with as swirl component, achieved through the use of an axial swirler, in the same direction of the rotation generated by the angled air jets from the top. Four hollow cone, pressure atomizers slightly retracted from the bottom plate are located at 0°, 90°, 180°, and 270° azimuthal positions. Sprays are injected normal to the bottom plate, creating a spray in cross-flow configuration, which is a key element of the liquid-fueled LEAF operation. Controlling the amount of the various air flows allows us to change the flame characteristics of the combustor and achieve ignition and stabilization of the flame over a range of operating conditions. The assessment of the optimal configuration of such flows with respect to the spray injection is part of this study. Further understanding of the relative effect of the various flows in terms of emission performance will generate a fundamental understanding to enable practical use of this novel technology.

To keep the temperature of the bottom and top stainless-steel plates sufficiently low for safe operation, external cooling is applied in the experiment (air cooling for the bottom plate and water cooling for the top plate). The presence of cooling flows could make the operation of the combustor far from ideal adiabatic combustion. To extend the experimental understanding to the ideal adiabatic configuration and, therefore, project the LEAF toward the use as a gas turbine technology, where advanced materials are used, numerical simulations with adiabatic walls are used. One should note that, as a result of the additional cooling used in the measurement campaign, results from experiments and those from simulations are not directly compared against each other in this work. Additionally, real gas turbine applications require specific cooling strategies, such as supplying air into the combustion chamber from film-cooled liners, which differ from the approach used in this work.

METHODS

In this section, the experimental procedures are described, followed by information on the visualization equipment and techniques and a discussion on the characterization of nanoparticles and exhaust gases. Then, the numerical approach and simulation setup used are given.

Experimental Procedures. The air mass flow rate of both the top jets and the core air are set using Alicat mass flow controllers. Air is obtained from a compressed air system and filtered with particulate and coalescent filters, and the pressure is set with a regulator. Air is injected at room temperature through all injection ports, that is, without any air preheating. The eight jets are arranged in a circle of 45 mm radius from the central axis, and each orifice is angled so that air is injected with a tangential component into the combustor. The injection angle between the direction of the top air jets and normal to the ceiling of the combustor is 30°. The core air flow swirl number is 1.3.

The liquid fuel is stored in a small reservoir at ambient temperature and pumped to the atomizers by a gear pump controlled by a Bronkhorst mass flow meter. Standard Jet A fuel is used; the specific fuel batch, Jet A fuel with "average" properties, was fully characterized in terms of chemical and thermophysical properties, as well as other characteristics, such as flame speed.[31−34] A stable operation of the LEAF flame was also achieved for fuels of higher volatility, such as ethanol and *n*-heptane. The four atomizers (hollow cone, 50° cone angle, and 90 μm orifice) are equally spaced around a 55 mm radius circle in relation to the central axis of the combustor, at the bottom surface. To ignite the kerosene spray, a premixed air−methane pilot flame is stabilized at the tangential pilots and blown-off by switching off the methane fuel, following the ignition of the main kerosene spray flame. Temperature and emission measurements at the outlet of the combustor as well as the visualization of the flame are carried out only once the temperature of the bottom part of the combustor reaches 140 °C.

The operating conditions investigated are given in Table 1 and concern two sets of experiments defined by the letters "J" and "C", referring to the variation of the top jet mass air flow rate ($\dot{m}_{jets}$) or the core air flow rate ($\dot{m}_{core}$), respectively. In each set of experiments, the respective air flow rate is varied, while the other two air flow rates are kept constant. The tangential air is set constant at 0.65 g/s using a Bronkhorst mass flow controller. The given flow rates resulted in velocities

https://dx.doi.org/10.1021/acs.energyfuels.0c03860
Energy Fuels 2021, 35, 7092−7106

Table 1. Experimental Conditions

number	$\dot{m}_{jets}$ (g/s)	$\dot{m}_{core}$ (g/s)	ϕ	$\dot{m}_f$ (g/s)
J1	3.54	0.79	0.70	0.245
J2	3.93	0.79	0.70	0.264
J3	4.33	0.79	0.70	0.285
J4	4.72	0.79	0.70	0.304
J5	5.11	0.79	0.70	0.326
C1	4.33	0	0.75	0.263
C2	4.33	0.39	0.75	0.283
C3	4.33	0.79	0.75	0.306
C4	4.33	1.18	0.75	0.325
C5	4.33	1.57	0.75	0.346

between 120 and 170 m/s at the top jets, between 0 and 1.5 m/s at the core flow, and 0.9 m/s at each tangential pilot operating only with cold air. The kerosene flow rate is varied to result in an overall (global) equivalence ratio, ϕ, of 0.7 and 0.75 for the "J" and "C" experiments, respectively.

For the sake of clarity, it should be noted that previous experiments with methane[8] considered an overall equivalence ratio range of 0.5−0.75, top air jet velocities in the range of 13−90 m/s, core air flow velocities of 0.4−2.5 m/s, and pilot air velocities in the range of 0.8−2.5 m/s. While a very similar range of tangential velocities and core air flow velocities were used in both the liquid-fueled and gas-fueled experiments, significantly higher velocities of the top jets were needed in the present work, almost twice as high as those in gaseous experiments. This is discussed later, in the Results and Discussion. Additionally, the lean operating limit of the LEAF was found to be approximately ϕ = 0.57−0.65 for the range of air flow conditions explored in the present work, while the methane LEAF allowed for somewhat leaner conditions (ϕ = 0.38−0.52). The issue of stability is also discussed later in light of the liquid-fueled injection characteristics.

Flame Visualization. Long-exposure still photography in the visible and high-speed imaging of the flame chemiluminescence and the natural luminescence of soot were used to characterize the flame in the combustor. The camera was pointed down into the combustor, to include the region close to the spray located just below the cylindrical quartz wall. A high-speed CMOS camera (Photron SA1.1) and a two-stage image intensifier (LaVision HS-IRO) with a 100 mm ultraviolet (UV) lens were used, with a 310 and 430 nm band-pass filter [10 mm full width at half maximum (fwhm)] used for the visualization of OH* and CH*, respectively, and a 570 nm long-pass filter for soot luminescence in the visible spectrum. As a result of the filter used and a camera with higher sensitivity in the visible spectrum, used for imaging soot luminescence, the luminescence of carbonaceous particles larger than 10 nm is expected to be visualized.[35,36] The imaging of the flow was carried out at 12 kHz with an exposure time of 60 μs. All imaging parameters of both the still camera and the high-speed camera (e.g., gain, aperture, and shutter speed) were kept the same across the different operating conditions, so that the intensity in the visualized wavelength or whole visible spectrum could be directly compared between conditions.

Emissions. A SMPS from TSI was used to measure the PSDs. The SMPS is composed of an electrostatic classifier (EC, model 3080), a nanodifferential mobility analyzer (nano-DMA, model 3085), an advanced aerosol neutralizer (model 3088), and an ultrafine condensation particle counter (UCPC, model 3025). The sample flow rate and the sheath flow rate for the UPCP were set at 1.5 and 15 L/min, respectively (high-flow operation mode), corresponding to a particle size range between 2.5 and 60 nm. The PSDs are the result of three independent and averaged acquisitions of 30 s for each operating condition, once the burner reached an operating temperature of 140 °C. Sampling was carried out at the center of the exhaust gas stream, at the outlet of the combustor, using a specific dilution probe for combustion product sampling. Additionally, temperature and emission measurements were carried out at the same position of the soot sampling, with a Testo 300 portable flue gas analyzer, which measures dry volume concentrations of O_2 (0−0.21 ± 0.002), CO (0−4000 ± 20 ppm), and NO (0−3000 ± 5 ppm).

Probe sampling has been widely used for measuring PSDs in combustion systems.[18,19,21,37] The dilution probe for the present work was specifically designed to be used at the exhaust as well as inside turbulent burners.[29] The probe consists of an inner stainless-steel tube (4 mm inner diameter) welded together with a coaxial outer stainless-steel tube (7 mm inner diameter) with a side pinhole of 0.5 mm diameter. Flame products are sampled through the pinhole as a result of a slight negative pressure gradient created by a vacuum pump downstream and immediately diluted with a nitrogen flow rate of 10 L/min. The overall dilution ratio (DR) was estimated to be 100 by extracting a portion of the mixture of exhaust gases diluted with N_2 before the DMA and analyzing the volume concentrations of each component in the mixture by gas chromatography mass spectrometry.[29] A precise control of the dilution ratio is provided by a needle valve, a pressure regulator, and a precision differential manometer placed downstream. The dilution ratio was high enough to reach and exceed critical dilution conditions, i.e., sampling conditions where any particle coagulation phenomenon in the line is avoided. The critical dilution ratio is reached once the shape of the size distribution is not affected by an increase in dilution, and the particle number changes with inverse proportionality to the amount of dilution.[18] Further, the PSDs were all corrected for the dilution ratio and for particle diffusion losses in the dilution probe and the sampling line, as discussed by Sgro et al.[20] and Minutolo et al.[38] The total experimental uncertainty for particle number density and volume fraction was evaluated as being ±20%, including the uncertainties deriving from the evaluation of DR.

Numerical Setup. The main objective of the numerical simulations is to provide additional information on the global characteristics of the time-averaged flow and mixing fields and demonstrate the combustor behavior in the ideal case of adiabatic combustion, which implies the use of advanced materials and coatings. The analysis of the mixing and reaction field has been conducted using Reynolds-averaged Navier−Stokes (RANS) simulations with a mixture fraction progress variable flamelet approach. Although more advanced numerical simulation and combustion models[39] are quite typical for the detailed analysis of the local flame structure, such as large eddy simulations combined with the online solution of chemistry, a less expensive computational approach was used in this work. This way, information on a wide range of conditions can be provided, together with an evaluation the global characteristics and trends of the flow field with changing operating conditions. Detailed analysis of the local flame structure will be addressed in future work. It should be noted that more advanced approaches are more sensitive to the definition of boundary

https://dx.doi.org/10.1021/acs.energyfuels.0c03860
Energy Fuels 2021, 35, 7092−7106

conditions and require further characterization of the experimental burner with respect to the heat transfer conditions of the walls.

The computational domain includes all of the main features of the combustor (Figure 3). Main and pilot air injection ducts

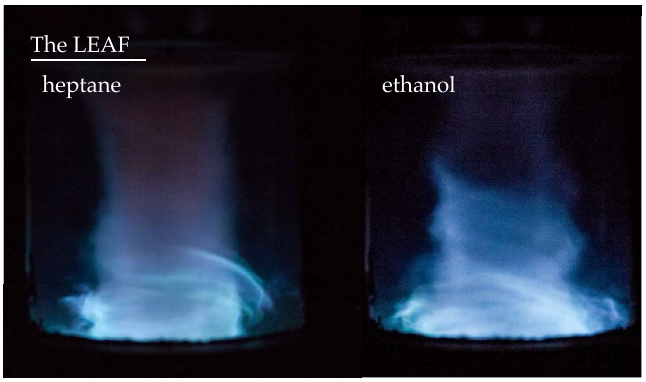

Figure 3. Schematic of the computational domain with main boundaries and a detail of the mesh in the vicinity of one of the air jets.

are included in the domain to allow for a fully developed flow at the injection section, which may have an impact on the overall jet dynamics and swirl component of the flow in the combustor. Inlet boundaries normal to the duct axis are employed. The experimental mass flow rate with uniform velocity is imposed at all of the air inlets. For the central air co-flow, a tangential velocity component is also imposed, following the geometrical angle of the swirler used in the experiment. The realizable $k-\varepsilon$ turbulence model[40] is used as a result of its better performance for the prediction of jets and swirling flows. Kerosene sprays are modeled using the Lagrangian approach for dilute sprays. The rapid mixing evaporation model[41] was used together with drag correlations for spherical droplets[42] for the computation of drag forces. All other forces acting on the droplets, including gravity, were neglected. Following the experimental setup, four hollow cone sprays are injected in correspondence with the bottom plate. The experimental fuel flow rate is imposed with droplet diameters sampled from a Rosin–Rammler distribution with a Sauter mean diameter equal to 20 μm and dispersion parameter equal to 3.0. Ambient temperature, T = 298 K, is used for both the droplets and the inlet air. A constant pressure condition is applied at the outlet, whereas all of the solid surfaces are modeled as no-slip adiabatic walls.

The turbulent combustion model used in this work is based on the use of tabulated flamelets. Turbulence effects on the mean flame are modeled using the presumed probability density function (PDF) approach based on the mixture fraction and progress variable. Presumed PDF flamelet methods have already been used in the context of spray flames and also moderate or intense low-oxygen dilution (MILD) conditions,[43−45] showing some success in the prediction of the mean behavior of the flame, even though further developments may be necessary to fully capture the dynamics and autoigniting characteristics of the local flame.[46−48] In this work, a progress variable based on CO_2, H_2O, and H_2 mass fractions is used.[44] It is assumed that the mixture fraction and progress variable are statistically independent. Their PDFs are assumed to have a β-function shape, which is computed from the respective Favre averages and variances. Transport equations are solved for the Favre-averaged mixture fraction $\tilde{\xi}$, progress variable $\tilde{c}$, and their respective variances $\widetilde{\xi''^2}$ and $\widetilde{c''^2}$. The flamelet table has been built using freely propagating flames computed with a detailed mechanism for kerosene.[49,50] Evaporation cooling is taken into account by solving a transport equation for the enthalpy with spray source terms and correcting the value of the temperature from the tabulated chemistry through the enthalpy defect. To evaluate the soot level, a semi-empirical two-equation soot model based on the solution of the soot mass fraction and soot number density[51] has been employed. The SIMPLE algorithm is employed for the pressure–velocity coupling. A fully tetrahedral mesh of about 12 million cells, refined in the high shear regions (see detail in Figure 3) and spray injection locations, is used. Second-order accurate discretization schemes are used for velocity, pressure, energy equation, and combustion-related quantities, whereas turbulence quantities, i.e. k and ε, are solved with first-order upwind schemes. Simulations were performed with the code PRECISE-UNS.[52] Cases C1–C5 have been simulated. Passive scalars, with the same transport properties as those of the mixture fraction, are also injected in correspondence with each of the air inlets to study the contribution of each air stream to the mixture formation.

RESULTS AND DISCUSSION

A successful operation of the LEAF concept with liquid–fuel injection was achieved for a range of fuels with significantly different volatilities, demonstrating the robustness of this concept. Figure 4 illustrates the operation of the combustor

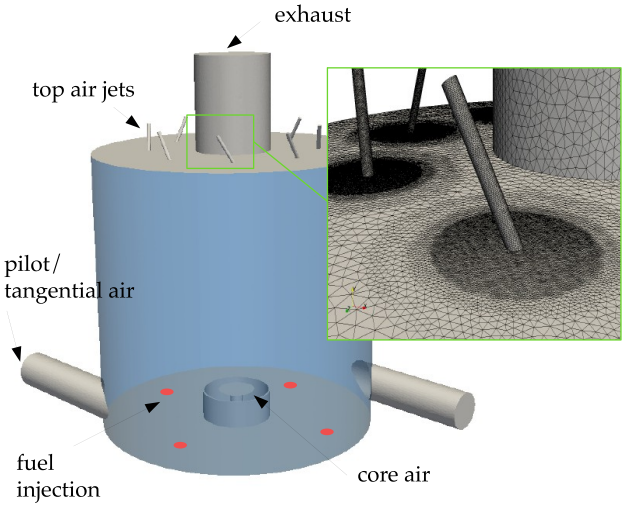

Figure 4. Short-exposure visible spectrum photography demonstrating the successful operation of the LEAF concept with heptane and ethanol injection. Air flows similar to those in condition J1 for kerosene were used, with an equivalence ratio of approximately 0.8.

with n-heptane and ethanol using (relatively) short-exposure photography in the visible spectrum. As a result of the higher volatility of these fuels in relation to kerosene, the toroidal reaction zone, characteristic of the LEAF, is located very close to the bottom surface, not being as clearly visualized in Figure 4 as it is in Figure 5 for kerosene operation. In the following sections, the general characteristics of the kerosene-fueled LEAF are discussed in terms of the flame characteristics and

https://dx.doi.org/10.1021/acs.energyfuels.0c03860
Energy Fuels 2021, 35, 7092−7106

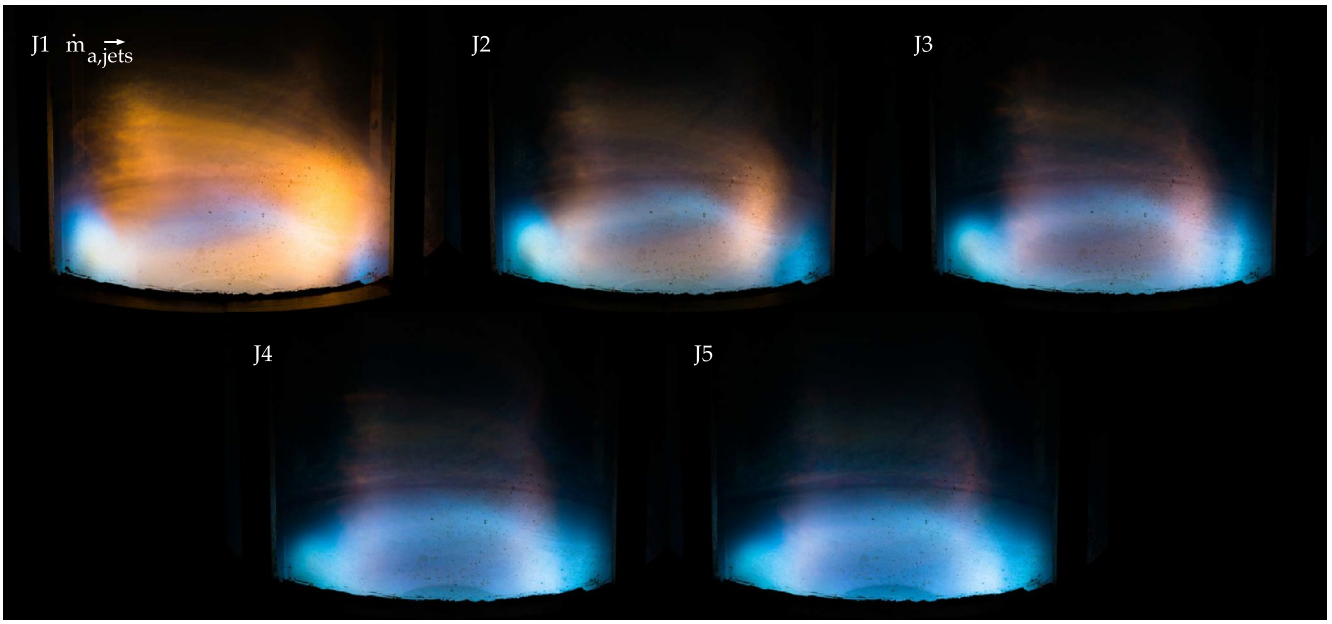

(a) varying $\dot{m}_{a,jets}$, ϕ_o=0.70.

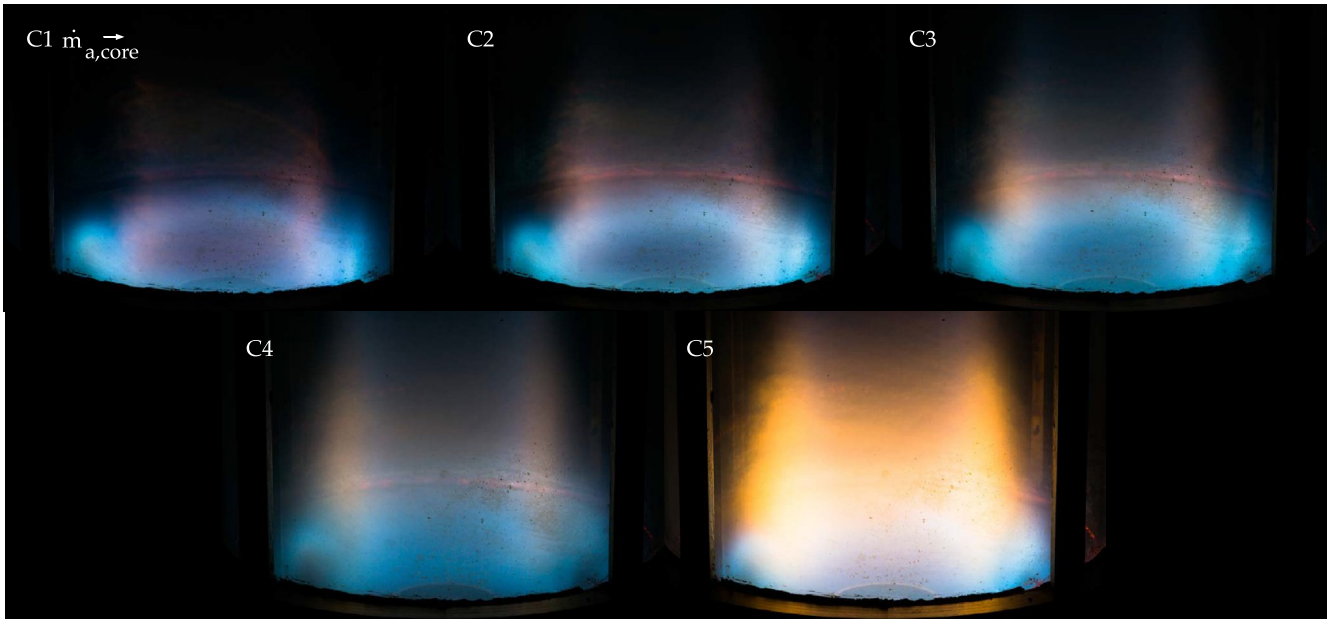

(b) varying $\dot{m}_{a,core}$, ϕ_o=0.75.

Figure 5. Long-exposure visible spectrum photography of the flame for (a) "J" experiments with varying $\dot{m}_{jets}$ and (b) "C" experiments with varying $\dot{m}_{core}$. At high $\dot{m}_{jets}$ and low $\dot{m}_{core}$, a clean flame with a very uniform bright-blue toroidal region is observed.

the resulting gas and particulate matter emissions for the range of operating conditions detailed previously, which consider a parametric investigation on the effect of air injection flow rates on the flame. This is followed by a discussion on the numerical results of the kerosene LEAF at adiabatic conditions, shedding light on more detailed flow issues of the concept, such as the aerodynamics of the combustor and mixing and reaction zone characteristics.

Flame Characteristics. The overall flame is seen in long-exposure still photographs in the visible spectrum of Figure 5. The "J" set of experiments is shown in panel a, in which the top air jet flow rates increased from J1 to J5, while "C" experiments are shown in panel b, with the core air flow rate increasing from C1 to C5. The reaction zone, depicted by the bright-blue toroidal region, was located close to the injection ports near the bottom of the combustor. The toroidal, azimuthal flame was formed even in the absence of a flame in both tangential pilots. For stabilization of the LEAF flame following ignition, the fuel in the pilots was reduced from stoichiometric to lean until blown off, while the injection of fresh air was kept constant. After the pilot flames were cut, a stable LEAF flame was still observed.

The stability mechanism of the LEAF has been discussed for gaseous fuels,[8] and an apparently identical mechanism was observed to apply to kerosene sprays, that is, the occurrence of the toroidal flame. This flame results from the sequential

https://dx.doi.org/10.1021/acs.energyfuels.0c03860
Energy Fuels 2021, 35, 7092−7106

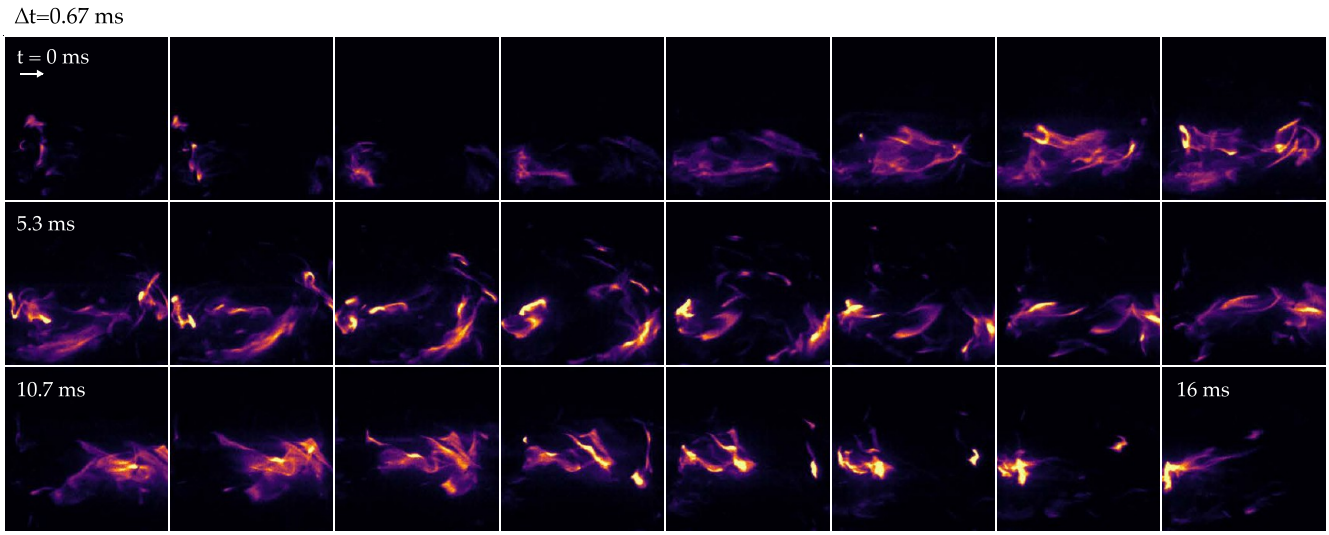

Figure 6. Image sequence of soot luminescence depicting the formation, growth, and further oxidation of soot as it undergoes a long whirling motion around the central axis of the combustor, before leaving the combustor. The time interval between frames is Δ = 0.67 ms − J1.

combustion of four individual sprays in the azimuthal direction as well as from the high amount of recirculation found in the axial direction. The verification of both a similar stabilization mechanism and the proximity of the flame to the bottom of the combustor were attributed to the fast evaporation of the spray, in addition to the fast mixing of the vapor fuel with air and entrained combustion products. The resulting high evaporation rates of the already fine droplets injected, in turn, resulted in very short time scales of full evaporation of the kerosene fuel. Also, high air jet velocities of up to 170 m/s are expected to induce high mixing in the combustor. Such velocities are about twice those found previously with gas operation[8] as a result of higher air flow rates used in the present work.

Such high flow rates of the top air jets, $\dot{m}_{jets}$, had a strong impact on the location and overall shape of the reaction zone. As $\dot{m}_{jets}$ increased from J1 to J5, the reaction zone became more attached to the bottom of the combustor and increasingly exhibited a more uniform ring-like structure (Figure 5a). At J5, a very uniform bright-blue ring is seen in the photographs, in contrast to visibly distinct interconnected flames seen in J2 and for gas operation.[8] This effect is associated with a decrease of the fuel penetration as $\dot{m}_{jets}$ increased, which occurred as a result of higher cross-flow velocities experienced by the spray. Additionally, it is clear that significantly less visible soot luminescence was achieved by increasing $\dot{m}_{jets}$ while keeping the global equivalence ratio ϕ constant. On the other hand, as air was introduced axially through the core injection port, a clear increase of soot luminescence was observed as the flame color changed to bright yellow at C5 (Figure 5b). This fact, however, did not significantly affect the amount of particulate matter measured at the outlet of the combustor. Further details on this behavior are given in the next section in light of size and number measurements of nanoparticles, showing that a soot-free condition at the combustor exhaust was achieved for all conditions studied.

Soot luminescence was intermittently observed for J1, J3, C1, and C3, while C5 (highest $\dot{m}_{core}$) exhibited a continuous sooting behavior and J5 (highest $\dot{m}_{jets}$) did not exhibit visible soot. Although intermittent, soot was observed to undergo a long whirling path in any of the investigated operating conditions. As seen in Figure 6, growth and further coagulation of soot seemed to occur initially within the first few milliseconds after a luminescence signal was first detected at the downstream most location. After a long whirling motion around the central axis of the combustor, the soot signal gradually decreased, indicating that such particles do not actually leave the combustor immediately after they are formed because they are, in fact, quickly oxidized before exiting. This is likely to occur as a result of the long residence times at O_2-rich conditions and high temperatures.

The flame structure and the soot-rich regions are shown in Figure 7 using instantaneous images of OH* and soot luminescence taken for all conditions studied. As $\dot{m}_{core}$ increased from zero to its maximum value from C1 to C5, OH* was observed over a longer axial length of the combustor (C5), as opposed to just close to the bottom plate (C1). The observed trend suggests that fuel escaped the toroidal reaction zone as air was increasingly introduced through the central core injection port, thus mixing and reacting with fresh air in that region rather than with high-temperature products and air from the top air jets.

A clear picture of the behavior described previously can be obtained from the time-averaged CH*, OH*, and soot luminescence images shown in Figure 8. From J1 to J5, not only was a more uniform flame structure observed at J5, as discussed previously, but also a significantly brighter OH* signal, which indicates a higher heat release within that region of the azimuthal flame. For C3 and C5 conditions, the high amount of CH* and OH* at the middle of the combustor seems to indicate the presence of a secondary reaction zone near the region where high soot luminescence was also observed. The increase of soot with increasing flow rate of the core flow is consistent with the simulations at adiabatic conditions, as discussed later in Figure 15. One should note that caution should be exercised when interpreting such images as a result of the line-of-sight character of the visualization.

Gas and Particulate Emissions. Figure 9 shows the gas species concentration and temperature measurements for (a) "J" experiments and (b) "C" experiments. Values of NO and CO are given in terms of 15% O_2 dilution as a standard

https://dx.doi.org/10.1021/acs.energyfuels.0c03860
Energy Fuels 2021, 35, 7092−7106

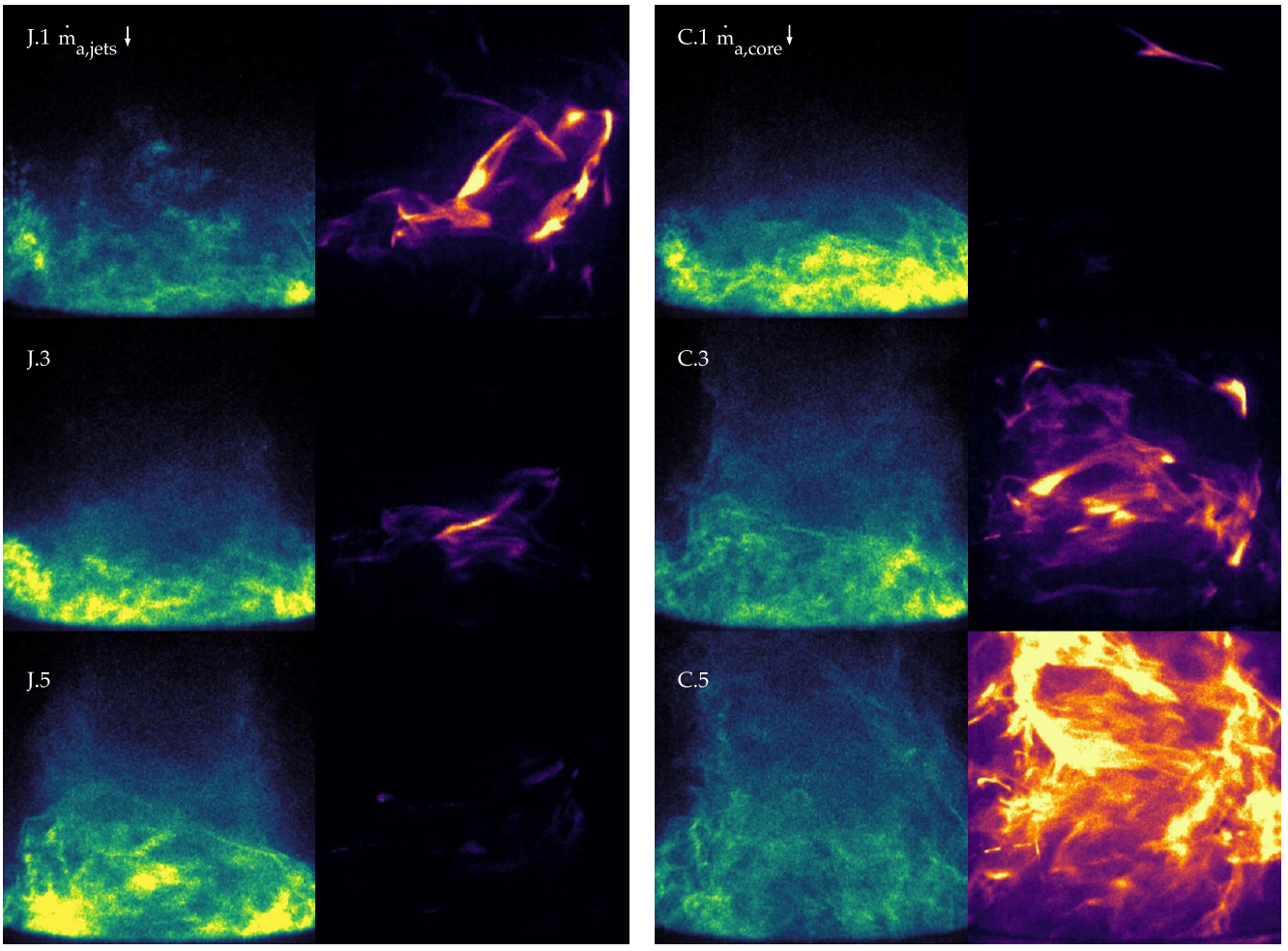

Figure 7. Instantaneous high-speed OH* and soot luminescence images representative of experiments (a) "J" with varying $\dot{m}_{jets}$ and (b) "C" with varying $\dot{m}_{core}$. The OH* images indicate the presence of a very fragmented reaction zone, located at the bottom part of the combustor. Soot seems to be formed near the vertical middle of the combustor, around the central rotating core, in the region between the central axis and the combustor walls.

(dashed line), in addition to the actual measured values (continuous line). From such measurements and knowing the injected equivalence ratio of the mixture, the amount of unburnt relative to the injected fuel mass $m_{f,u}/m_{f,u}$ was directly estimated from an atomic balance using the global reaction equation for combustion of kerosene, assuming its average molecular formula. This is given in Figure 10 together with the effective equivalence ratio $\phi_{eff} = \phi(1 - m_{f,u}/m_f)$. As discussed previously, increasing the air flow rate in either J or C experiments was accompanied by an increase in $\dot{m}_f$, so that ϕ was kept constant. Still, two distinct behaviors were observed. Increasing $\dot{m}_{jets}$ from J1 to J5 led to a higher amount of relative unburnt fuel, while the opposite was observed as $\dot{m}_{core}$ increased from C1 to C5. Effectively, this shows that the reaction occurred in a significantly leaner mixture in J5 and C1 experiments than in J1 and C5, respectively, explaining the low CO_2 values and low temperatures measured in those conditions as well as low NO_x levels.

The presence of relatively high amounts of unburnt fuel is attributed to both the injection direction and the characteristics of the hollow cone atomizer. It seems to be the case that, because part of the spray is directed radially inward toward the center of the combustor as a result of the 50° cone angle of the atomizers, the droplets are diverted from the main reaction zone, vaporizing as they approach the central axis of the combustor without burning. There, they mostly mix with combustion products (at low core air flow rates), quickly exiting the burner. As the core air flow rate is increased from C1 to C5, more oxidizer is available in the central region; thus, the gaseous fuel mixes and reacts, creating a secondary reaction zone in that region, as discussed further in the context of soot visualization and also in the numerical findings. To address the high amount of unburnt fuel at both J5 and C1 operating conditions while still keeping the effective equivalence ratio lean, the fuel atomization, spray angle, and injection location must be optimized in future designs of the combustor.

The number PSDs measured at the exhaust of the LEAF burner are reported in Figure 11, together with the PSDs for a standard and RQL-diluted non-premixed ethylene flame,[8] given as a reference. For all of the experimental conditions, the highest number concentration of nanoparticles is measured for particle diameters below 5 nm. With an increasing particle size,

https://dx.doi.org/10.1021/acs.energyfuels.0c03860
Energy Fuels 2021, 35, 7092−7106

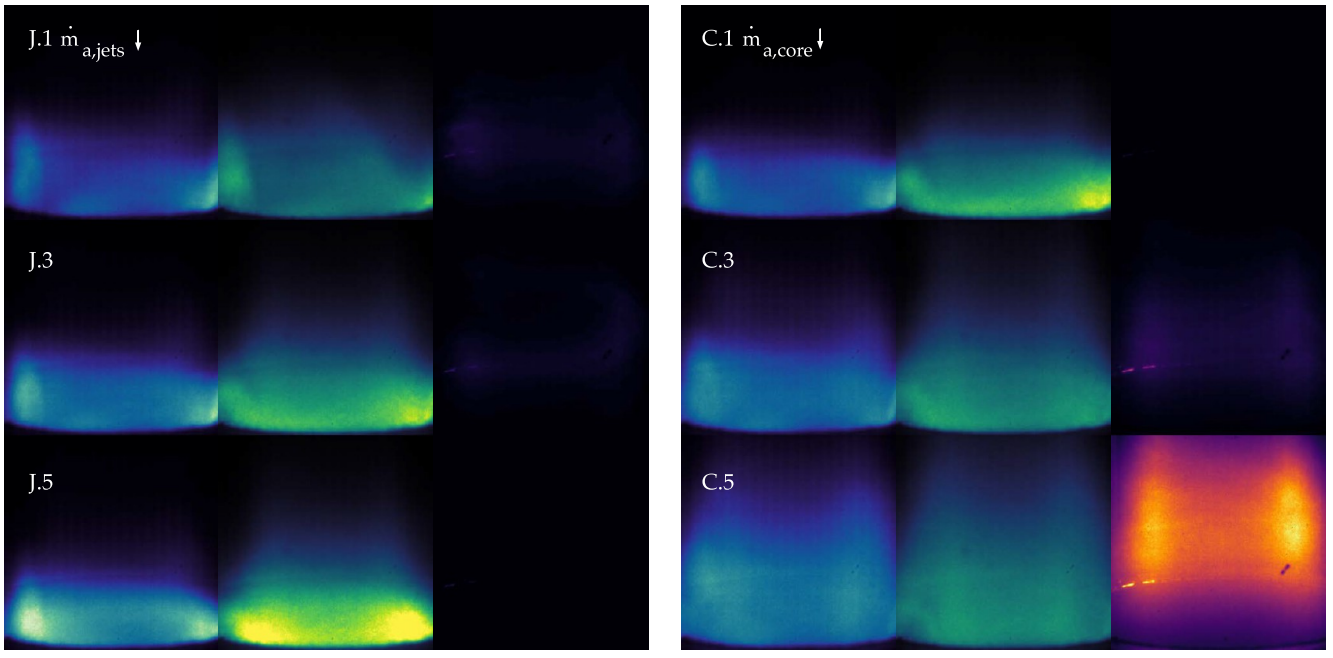

(a) varying $\dot{m}_{a,jets}$, ϕ_o=0.70. (b) varying $\dot{m}_{a,core}$, ϕ_o=0.75.

Figure 8. Time averages of high-speed OH*, CH*, and soot luminescence image sequences of (a) "J" experiments with varying $\dot{m}_{jets}$ and (b) "C" experiments with varying $\dot{m}_{core}$. The presence of OH* is observed mostly at the bottom part of the combustor, increasing in the axial coordinate as more air is injected through the core. This process also enhances the formation of soot within the combustor.

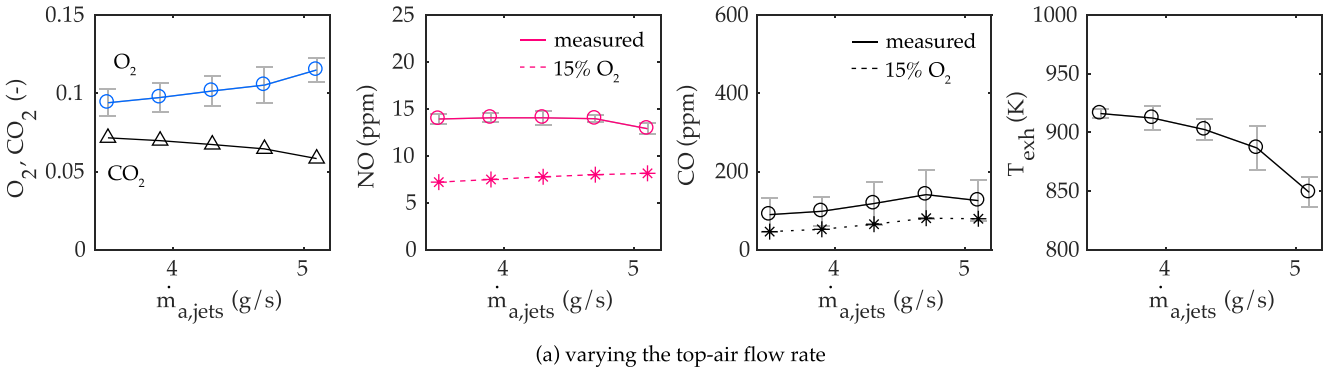

(a) varying the top-air flow rate

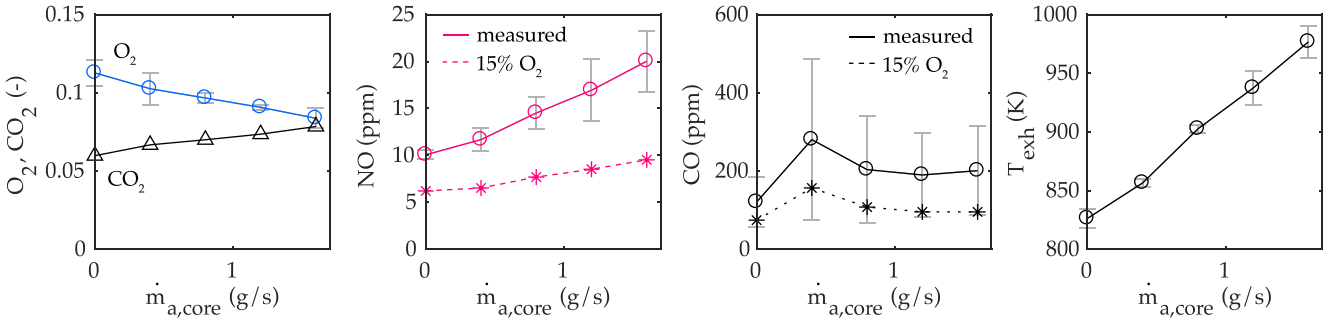

(b) varying the core-air flow rate

Figure 9. Measured gas volume fractions at the combustor exhaust for experiments with (a) varying top jet air flow rate $\dot{m}_{jets}$ and (b) core air flow rate $\dot{m}_{core}$, i.e., J and C operating conditions, respectively.

https://dx.doi.org/10.1021/acs.energyfuels.0c03860
Energy Fuels 2021, 35, 7092−7106

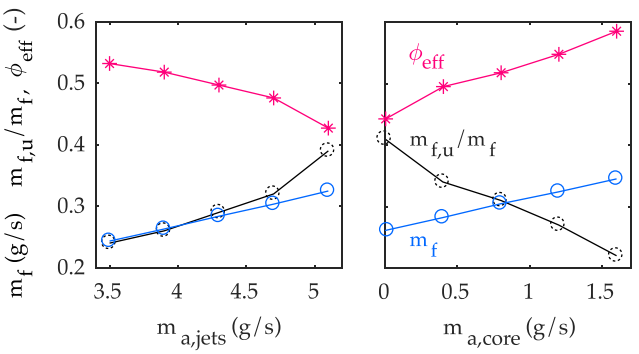

Figure 10. Measured fuel mass flow rate and calculated unburnt fuel ratio and effective equivalence ratio for both (left) J and (right) C operating conditions.

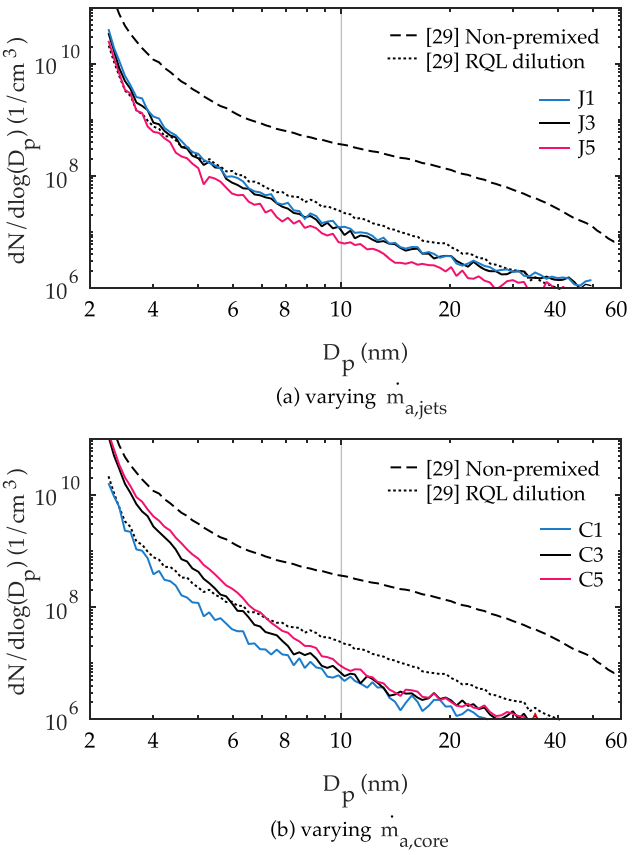

Figure 11. PSD at the outlet measured while varying the (a) top jet air flow rate and (b) core air flow rate (conditions J and C, respectively). The PSDs for the standard and RQL-diluted non-premixed ethylene flame from ref 29 are given as a reference.

the number concentration tends to decrease and becomes almost negligible for particles of 10 nm or greater. Within the experimental uncertainties, PSDs measured for the "J" experiments (Figure 11a) are identical and overlap with the PSD measured for the cleanest RQL-diluted non-premixed ethylene flame, suggesting that the variation of the top jet mass airflow rate did not significantly affect nanoparticle emissions at the exhaust. The measured trend is similar to that of the RQL-diluted non-premixed ethylene flame, but a significantly lower amount of particles is produced. As previously stated, it is likely that soot particles were produced inside the combustor, although they were not detected at the exhaust because they experience long residence times at O_2-rich conditions and high temperatures, resulting from a combination of recirculation and oxidation processes. Figure 11b shows the PSDs measured for the "C" experiments. Within the experimental uncertainties, the C1 flame is characterized by particle emissions identical to that of J1−J5 flames, while a slightly higher amount of the particle number concentration can be observed for C3 and C5 flames in the dimensional range below 6 nm. It seems to be that the increase of the core air flow rate resulted in a more continuous sooting behavior inside the combustor, as shown from soot luminescence imaging, and, in turn, in a higher amount of smallest particles deriving from the recirculation and oxidation processes.

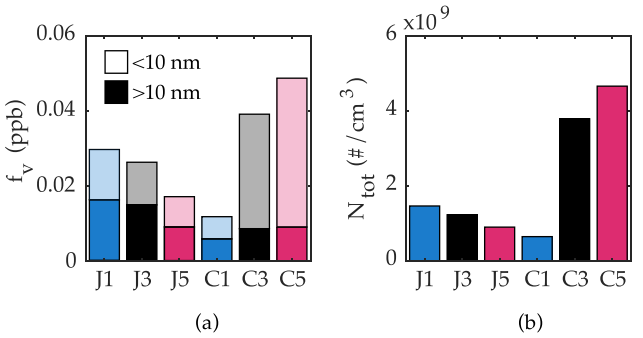

Figure 12. Measured (a) total soot volume fraction (with contributions from particles of size less and greater than 10 nm) and (b) total number density.

Figure 12 shows particle number density N_{tot} and particle volume fraction f_v derived from PSDs in Figure 11. Both quantities confirm all findings obtained from the analysis of the PSDs. The slight differences measured for C3 and C5 PSDs result in an increase of N_{tot} and f_v. Such an increase is higher for N_{tot} because a slightly higher amount of the particle number concentration was measured in the smallest dimensional range, thus contributing more in terms of the particle number rather than the particle volume. All of the experimental conditions investigated in the LEAF burner are characterized by $f_v < 0.5$ ppb and $N_{tot} < 5 \times 10^9$ numbers/cm^3 and can be considered as non-sooting and low-nanoparticle emitting flames, suggesting that the LEAF technology is certainly suitable to be applied for realizing a low particle emission combustor.

Aerodynamic Characteristics. The flow configuration is investigated here by means of simulations at adiabatic conditions. Residence times in the range of 65−85 ms were found for the range of conditions investigated. The three-dimensional flow field is examined in Figure 13, showing multiple streamlines seeded from inside one of the high-pressure top air jets. A whirling motion of pure air, as characterized by mixture fraction values close to 0, is created as a result of the high axial and radial momentum induced by the jets. During the descent, both the mixture fraction and temperature of the stream begin to increase gradually (cf. Figure 15), indicating air vitiation from the mixing with burnt combustion products. The stream is progressively vitiated, and only a small perimeter of pure air in close proximity to the combustor wall remains. The vitiated oxidizer stream reaches the bottom plate of the combustor after an approximately 180°

https://dx.doi.org/10.1021/acs.energyfuels.0c03860
Energy Fuels 2021, 35, 7092−7106

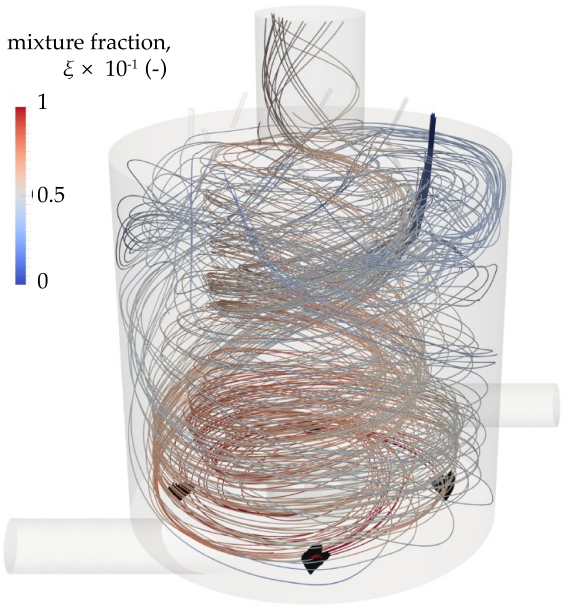

Figure 13. Streamlines seeded from one of the top jets and colored by the mixture fraction for case C5. The fuel spray injection is visualized by black isosurfaces of the liquid volume fraction equal to 1×10^{-4}.

rotation about the central burner axis. Here, the liquid fuel spray is injected in the form of a hollow cone. The kerosene droplets evaporate rapidly, within about 30 mm above the injection plane (Figure 16), as a result of the high-temperature environment. The gaseous fuel released subsequently mixes with the vitiated oxidizer stream, significantly increasing the local mixture fraction. Small amounts of fresh air are added to the mixture from the two tangential inflow pipes. The mixture of vitiated air and kerosene ignites and forms a reaction zone swirling around the central burner axis. The resulting hot combustion products increase the local gas temperature. Finally, these products are convected back up toward the exhaust pipe, further vitiating and preheating the incoming oxidizer stream on its way down.

The mean axial and tangential velocity components are quantified in Figure 14. Between the different cases C1, C3, and C5, the overall shape of the velocity field remains roughly the same. A white isocontour indicates the location of the vertical shear layer between the oxidizer stream and the burnt products.

Reaction Zone and Mixing. The mean temperature field and soot concentration are shown in Figure 15. High temperature levels are sustained throughout the combustor as a result of the adiabatic wall conditions applied in the simulation, preventing any heat transfer to the surroundings. These conditions also prevent any unburnt fuel from reaching the exhaust; 20−40% unburnt fuel is observed in experiments, where strong cooling of the combustor is applied. Further, overall lower temperatures are obtained in the simulations when increasing the core air mass flow rate (from C1 to C5). This effect is possibly due to the additional cold air dilution or evaporative cooling of droplets attracted to that region, as discussed previously. Soot production, on the other hand, increases from C1 to C5 in agreement with the measurements. This is likely caused by the higher fuel mass flow rate used to keep the global equivalence ratio constant. Figure 17 shows, accordingly, a local increase of the mixture fraction in the fuel injection region, representing a richer mixture, which also provides more favorable conditions for soot formation. The variance of the mixture fraction indicates intense fuel mixing close to the injection location, which is related to the strong evaporation in that region. In fact, as also shown in Figure 16, the spray strongly interacts with the swirling cross flow and completes the evaporation close to the injection location. The core air is therefore not expected to reach the main reaction zone and contribute significantly to the mixture formation and combustion process in the vicinity of the spray. Indeed, numerical results using three passive scalars, each injected from a different type of air inflow stream (top jets, core, and pilot), indicate that most of the core air is entrained within the central column of mainly burnt products. This lack of radial expansion is clearly visible in Figure 18, which shows the dilution of two of the passive scalars. However, the stoichiometric mixture fraction isoline shown in Figure 17 suggests that the injection of the core flow air leads to the formation of a secondary reaction close to the combustor axis, resulting in a toroidal shape of the reaction zone. Numerical simulations show that, in the limiting case of adiabatic walls, full evaporation of the spray can be achieved. At the same time, numerical simulations demonstrate that the LEAF configuration allows for achievement of an intense mixing with the hot products and a relatively homogeneous mixture in most of the volume of the burner, apart from the region in the vicinity of the spray

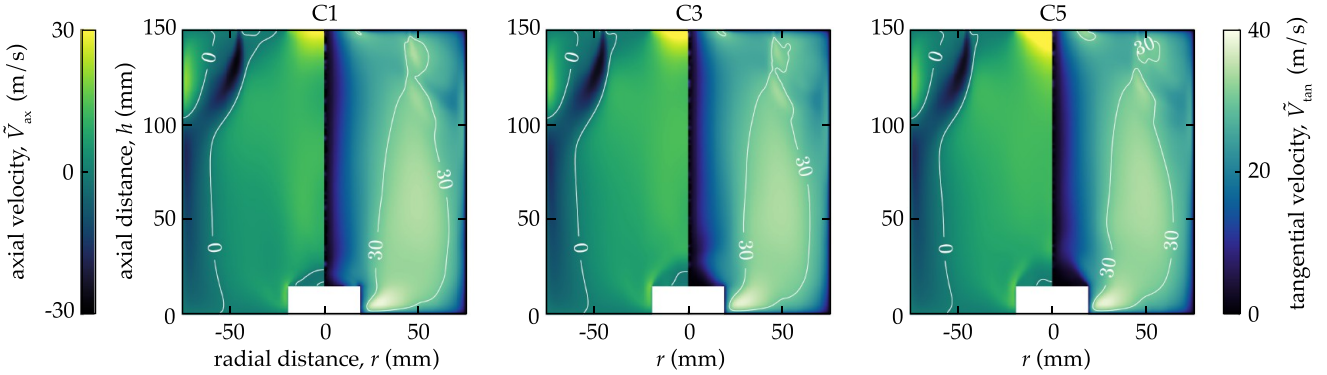

Figure 14. Axial (left half) and tangential (right half) velocity components, $\tilde{V}_{ax}$ and $\tilde{V}_{tan}$. The quantities have been obtained through an azimuthal average around the axis of the combustor.

https://dx.doi.org/10.1021/acs.energyfuels.0c03860
Energy Fuels 2021, 35, 7092−7106

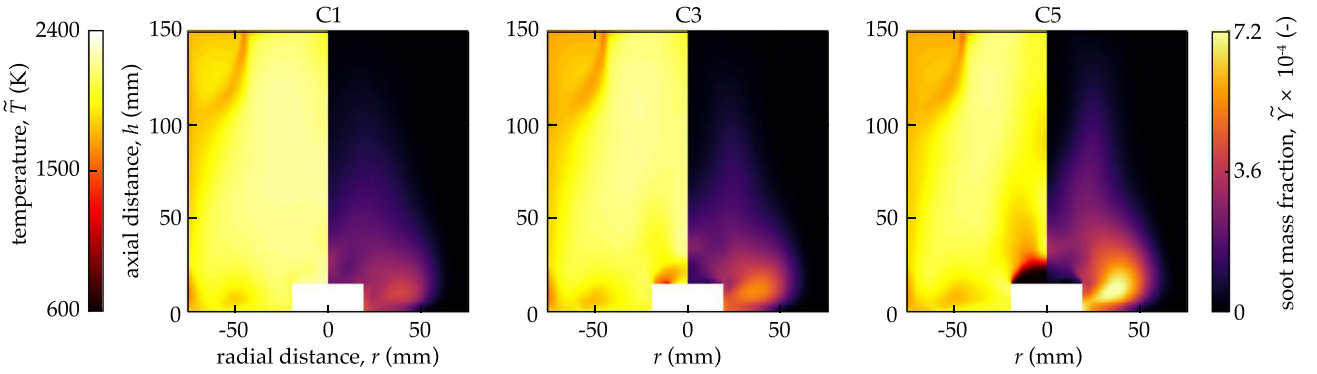

Figure 15. Temperature $\tilde{T}$ (left half) and soot mass fraction $\tilde{Y}_{soot}$ (right half). The quantities have been obtained through an azimuthal average around the axis of the combustor.

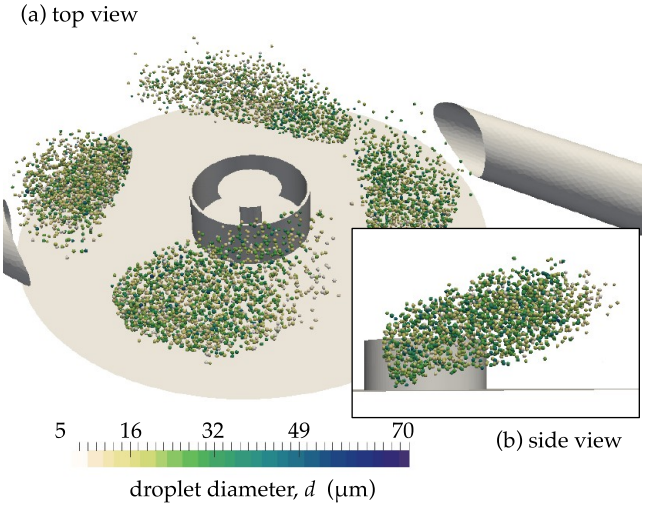

Figure 16. Visualization of the spray predicted by numerical simulations for the condition C5. The side view (b) shows only the droplets injected by a selected injector.

injection. The presence of an extended area with a stoichiometric mixture observed in the computations could be avoided by decreasing the fuel flow rate (note that the effective equivalence ratio of the experiment is expected to be lower compared to the nominal value as a result of unburnt fuel at the exhaust, as previously discussed).

Again, one should note that the combustor presented in this study should be regarded as a proof of concept. Future work will focus on configurations closer to real applications, for example, by including realistic cooling flows (e.g., from film-cooled liners) and walls (e.g., with ceramic coatings) as well as optimized injection configurations. Additionally, new strategies to reduce the high-pressure drop associated with the high-momentum air jets will also be pursued. Finally, current experiments were carried out at atmospheric conditions, while new tests at high-pressure conditions should be further explored as part of the development and establishment of the LEAF technology toward practical applications.

CONCLUSION

The LEAF combustion concept was observed for the first time with kerosene sprays. Experiments and simulations demonstrated the existence of a nominally diffusion-type kerosene system that has zero soot and produces very low levels of NO_x and CO, showing a promising combustor concept for the next generation of ultralow-emission aeroengines.

In relation to the aerodynamics, mixing, and reaction zones of the combustor, the key findings are as follows. First, air injected through the top orifices induced a strong whirling motion of the flow around the central axis of the combustor. Second, air moved radially outward from the top orifices and from top to bottom, gradually entraining combustion products toward the reaction zone. Third, a toroidal reaction zone was located near the bottom of the combustor, with the reaction

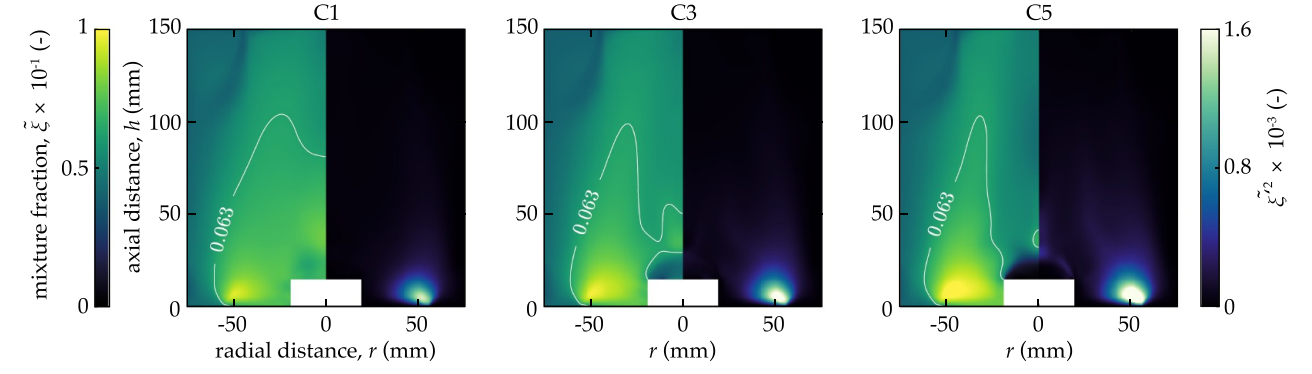

Figure 17. Mixture fraction $\tilde{\xi}$ (left half) and its variance $\widetilde{\xi''^2}$ (right half) including an isocontour of the stoichiometric mixture fraction, $\tilde{\xi}_{stoi} = 0.063$. The quantities have been obtained through an azimuthal average around the axis of the combustor.

https://dx.doi.org/10.1021/acs.energyfuels.0c03860
Energy Fuels 2021, 35, 7092−7106

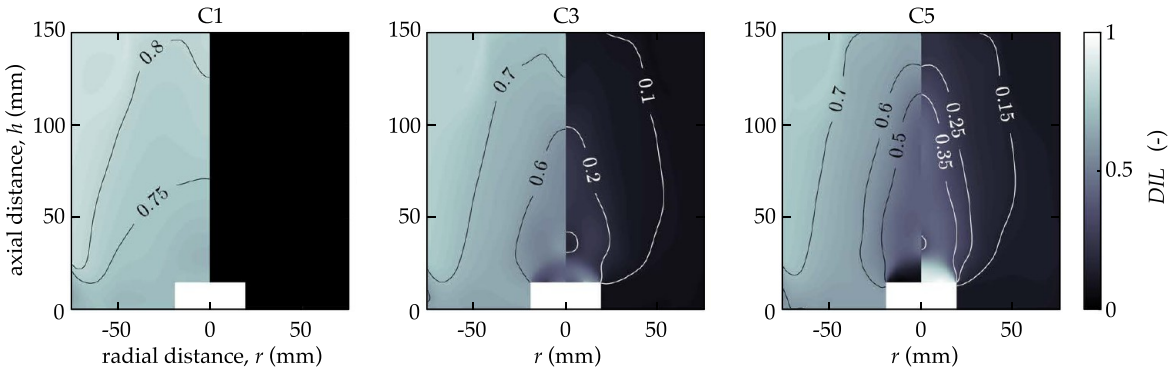

Figure 18. Two passive scalars injected, respectively, from the top jets (left half) and central core (right half) to visualize the dilution of both streams within the combustor. Note that a third scalar representing the pilot air stream is not shown here. The quantities have been obtained through an azimuthal average around the axis of the combustor.

occurring between the fuel and vitiated air. This followed the same stabilization mechanism of the gaseous LEAF, that is, sequential ignition of each spray as a result of the high amount of products recirculated and entrained by the top air jets. Fourth, air injected through the core port (bottom-center part) did not seem to participate in the main reaction zone. Still, combustion also occurred near the core region, mostly with a fresh oxidizer, as indicated by both numerical results and an increase in CH* and OH*, visualized across the axial direction. Finally, increasing the top air jet flow rate led to a very uniform toroidal reaction zone, closely attached to the bottom of the combustor. At such conditions, the highest intensity levels of CH* and OH* were observed, with virtually zero soot luminescence within the burner.

Regarding the overall thermal and emissions performance of the burner, the following points are highlighted. First, as a result of reactions occurring with fresh air at fuel-rich conditions near the central axis, high soot luminescence was observed in the experiments and a high soot mass fraction was evaluated in the simulations. The total soot volume fraction and absolute number of particles in the 2−10 nm range measured at the outlet increased as the amount of core injection air increased. Second, an increase of air injection in that region also led to a lower amount of unburnt hydrocarbons, higher temperatures, and NO_x and CO emissions. Third, in average- to high-sooting cases, a reduction of soot luminosity occurred downstream, near the top of the combustor. This was associated with soot oxidization occurring as a result of entrainment of fresh air (from the top jets) into the product stream and was observed in both experiments and simulations. This process is likely to occur even in the soot-free conditions, resulting in extremely low number concentrations of 2−10 nm nanoparticles measured in the exhaust.

Further experiments must be carried out with more realistic walls, such as ceramic coatings, to better reflect a realistic implementation in an aviation gas turbine. In the present work, significantly high cooling was needed to avoid high temperatures of combustor parts. Numerical simulations were then used to extrapolate the results obtained for the high-cooling conditions to more realistic adiabatic conditions. Further, additional *in situ* measurements of soot must be performed, and various spray configurations must be tested, to further optimize the combustor. More advanced numerical simulations should also be performed to further investigate the local flame structure and evaporation effects on combustion characteristics.

AUTHOR INFORMATION

Corresponding Author

Pedro M. de Oliveira − *Hopkinson Laboratory, Department of Engineering, University of Cambridge, Cambridge CB2 1PZ, United Kingdom;* orcid.org/0000-0002-5527-8128; Email: pm580@cam.ac.uk

Authors

Daniel Fredrich − *Department of Mechanical Engineering, Imperial College London, London SW7 2AZ, United Kingdom;* orcid.org/0000-0003-2207-4679

Gianluigi De Falco − *Dipartimento di Ingegneria Chimica, dei Materiali e della Produzione Industriale, Università degli Studi di Napoli Federico II, 80125 Napoli, Italy;* orcid.org/0000-0001-5116-3991

Ingrid El Helou − *Hopkinson Laboratory, Department of Engineering, University of Cambridge, Cambridge CB2 1PZ, United Kingdom;* orcid.org/0000-0001-6347-181X

Andrea D'Anna − *Dipartimento di Ingegneria Chimica, dei Materiali e della Produzione Industriale, Università degli Studi di Napoli Federico II, 80125 Napoli, Italy;* orcid.org/0000-0001-9018-3637

Andrea Giusti − *Department of Mechanical Engineering, Imperial College London, London SW7 2AZ, United Kingdom;* orcid.org/0000-0001-5406-4569

Epaminondas Mastorakos − *Hopkinson Laboratory, Department of Engineering, University of Cambridge, Cambridge CB2 1PZ, United Kingdom;* orcid.org/0000-0001-8245-5188

Complete contact information is available at: https://pubs.acs.org/10.1021/acs.energyfuels.0c03860

Notes

The authors declare no competing financial interest.

ACKNOWLEDGMENTS

The authors kindly acknowledge the financial support of the European Commission through the Clean Sky 2 Joint Undertaking under the European Union's Horizon 2020 Research and Innovation Program, Project LEAFINNOX (Grant Agreement 831804) and also thank Dr. J. T. Edwards

https://dx.doi.org/10.1021/acs.energyfuels.0c03860
Energy Fuels 2021, 35, 7092−7106

at the U.S. Air Force Research Laboratory for providing the fuel used in the experiments.

DEDICATION

This paper is dedicated to the memory of Professor Mário Costa. The authors of this work are grateful for all fruitful interactions that they had with Mário Costa over the years, whose passion for combustion science, dedication and service to the community, and legacy to the field, including the understanding of flameless oxidation, have been instrumental to our progress.

REFERENCES

(1) Liu, Y.; Sun, X.; Sethi, V.; Nalianda, D.; Li, Y.-G.; Wang, L. Review of modern low emissions combustion technologies for aero gas turbine engines. *Prog. Aerosp. Sci.* **2017**, *94*, 12−45.
(2) Nemitallah, M. A.; Rashwan, S. S.; Mansir, I. B.; Abdelhafez, A. A.; Habib, M. A. Review of Novel Combustion Techniques for Clean Power Production in Gas Turbines. *Energy Fuels* **2018**, *32*, 979−1004.
(3) Zhang, C.; Hui, X.; Lin, Y.; Sung, C.-J. Recent development in studies of alternative jet fuel combustion: Progress, challenges, and opportunities. *Renewable Sustainable Energy Rev.* **2016**, *54*, 120−138.
(4) Correa, S. M. A Review of NO_x Formation under Gas-Turbine Combustion Conditions. *Combust. Sci. Technol.* **1993**, *87*, 329−362.
(5) Cavaliere, A.; de Joannon, M. Mild Combustion. *Prog. Energy Combust. Sci.* **2004**, *30*, 329−366.
(6) Wünning, J. Flameless oxidation to reduce thermal no-formation. *Prog. Energy Combust. Sci.* **1997**, *23*, 81−94.
(7) Perpignan, A. A.; Gangoli Rao, A.; Roekaerts, D. J. Flameless combustion and its potential towards gas turbines. *Prog. Energy Combust. Sci.* **2018**, *69*, 28−62.
(8) El Helou, I.; Foale, J.; Giusti, A.; Sidey, J. A. M.; Mastorakos, E. Experimental and numerical investigation of an ultra-low NO_x methane reactor. *Energy Procedia* **2017**, *120*, 214−221.
(9) Hobbs, J. MILD combustion of sprays. Ph.D. Thesis, University of Cambridge, Cambridge, U.K., 2016.
(10) Xing, F.; Kumar, A.; Huang, Y.; Chan, S.; Ruan, C.; Gu, S.; Fan, X. Flameless combustion with liquid fuel: A review focusing on fundamentals and gas turbine application. *Appl. Energy* **2017**, *193*, 28−51.
(11) Zizin, A.; Lammel, O.; Severin, M.; Ax, H.; Aigner, M. Development of a jet-stabilized low-emission combustor for liquid fuels. *Proceedings of the ASME Turbo Expo 2015: Turbine Technical Conference and Exposition*; Montreal, Quebec, Canada, June 15−19, 2015; Paper GT2015-42642, DOI: 10.1115/GT2015-42642.
(12) Gounder, J. D.; Zizin, A.; Lammel, O.; Aigner, M. Spray Characteristics Measured in a New FLOX® Based Low Emission Combustor for Liquid Fuels Using Laser and Optical Diagnostics. *Proceedings of the ASME Turbo Expo 2016: Turbomachinery Technical Conference and Exposition*; Seoul, South Korea, June 13−17, 2016; Paper GT2016-56629, DOI: 10.1115/GT2016-56629.
(13) Reddy, V. M.; Trivedi, D.; Kumar, S. Experimental investigations on lifted spray flames for a range of coflow conditions. *Combust. Sci. Technol.* **2012**, *184*, 44−63.
(14) Mahendra Reddy, V.; Sawant, D.; Trivedi, D.; Kumar, S. Studies on a liquid fuel based two stage flameless combustor. *Proc. Combust. Inst.* **2013**, *34*, 3319−3326.
(15) Reddy, V. M.; Katoch, A.; Roberts, W. L.; Kumar, S. Experimental and numerical analysis for high intensity swirl based ultra-low emission flameless combustor operating with liquid fuels. *Proc. Combust. Inst.* **2015**, *35*, 3581−3589.
(16) Sharma, S.; Pingulkar, H.; Chowdhury, A.; Kumar, S. A new emission reduction approach in MILD combustion through asymmetric fuel injection. *Combust. Flame* **2018**, *193*, 61−75.
(17) Sharma, S.; Chowdhury, A.; Kumar, S. A novel air injection scheme to achieve MILD combustion in a can-type gas turbine combustor. *Energy* **2020**, *194*, 116819.
(18) Maricq, M. M.; Harris, S. J.; Szente, J. J. Soot size distributions in rich premixed ethylene flames. *Combust. Flame* **2003**, *132*, 328−342.
(19) Zhao, B.; Yang, Z.; Wang, J.; Johnston, M. V.; Wang, H. Analysis of soot nanoparticles in a laminar premixed ethylene flame by scanning mobility particle sizer. *Aerosol Sci. Technol.* **2003**, *37*, 611−620.
(20) Sgro, L. A.; D'Anna, A.; Minutolo, P. Charge fraction distribution of nucleation mode particles: New insight on the particle formation mechanism. *Combust. Flame* **2011**, *158*, 1418−1425.
(21) Abid, A. D.; Tolmachoff, E. D.; Phares, D. J.; Wang, H.; Liu, Y.; Laskin, A. Size distribution and morphology of nascent soot in premixed ethylene flames with and without benzene doping. *Proc. Combust. Inst.* **2009**, *32*, 681−688.
(22) Camacho, J.; Lieb, S.; Wang, H. Evolution of size distribution of nascent soot in n- and i-butanol flames. *Proc. Combust. Inst.* **2013**, *34*, 1853−1860.
(23) Conturso, M.; Sirignano, M.; D'Anna, A. Effect of 2,5-dimethylfuran doping on particle size distributions measured in premixed ethylene/air flames. *Proc. Combust. Inst.* **2017**, *36*, 985−992.
(24) Kazemimanesh, M.; Moallemi, A.; Olfert, J. S.; Kostiuk, L. W. Probe sampling to map and characterize nanoparticles along the axis of a laminar methane jet diffusion flame. *Proc. Combust. Inst.* **2017**, *36*, 881−888.
(25) Boyette, W.; Chowdhury, S.; Roberts, W. Soot Particle Size Distribution Functions in a Turbulent Non-Premixed Ethylene-Nitrogen Flame. *Flow, Turbul. Combust.* **2017**, *98*, 1173−1186.
(26) Chowdhury, S.; Boyette, W. R.; Roberts, W. L. Time-averaged probability density functions of soot nanoparticles along the centerline of a piloted turbulent diffusion flame using a scanning mobility particle sizer. *J. Aerosol Sci.* **2017**, *106*, 56−67.
(27) Abid, A. D.; Heinz, N.; Tolmachoff, E. D.; Phares, D. J.; Campbell, C. S.; Wang, H. On evolution of particle size distribution functions of incipient soot in premixed ethylene-oxygen-argon flames. *Combust. Flame* **2008**, *154*, 775−788.
(28) Commodo, M.; Tessitore, G.; De Falco, G.; Bruno, A.; Minutolo, P.; D'Anna, A. Further details on particle inception and growth in premixed flames. *Proc. Combust. Inst.* **2015**, *35*, 1795−1802.
(29) De Falco, G.; Helou, I. E.; de Oliveira, P. M.; Sirignano, M.; Yuan, R.; D'Anna, A.; Mastorakos, E. Soot particle size distribution measurements in a turbulent ethylene swirl flame. *Proc. Combust. Inst.* **2020**, *000*, 1−9.
(30) Gkantonas, S.; Sirignano, M.; Giusti, A.; D'Anna, A.; Mastorakos, E. Comprehensive soot particle size distribution modelling of a model Rich-Quench-Lean burner. *Fuel* **2020**, *270*, 117483.
(31) Colket, M.; et al. Overview of the National Jet Fuels Combustion Program. *AIAA J.* **2017**, *55*, 1087−1104.
(32) Edwards, J. T. Reference Jet Fuels for Combustion Testing. *Proceedings of the 55th AIAA Aerospace Sciences Meeting*; Grapevine, TX, Jan 9−13, 2017; DOI: 10.2514/6.2017-0146.
(33) Wang, K.; Xu, R.; Parise, T.; Shao, J.; Movaghar, A.; Lee, D. J.; Park, J.-W.; Gao, Y.; Lu, T.; Egolfopoulos, F. N.; Davidson, D. F.; Hanson, R. K.; Bowman, C. T.; Wang, H. A physics-based approach to modeling real-fuel combustion chemistry—IV. HyChem modeling of combustion kinetics of a bio-derived jet fuel and its blends with a conventional Jet A. *Combust. Flame* **2018**, *198*, 477−489.
(34) de Oliveira, P. M.; Mastorakos, E. Mechanisms of flame propagation in jet fuel sprays as revealed by OH/fuel planar laser-induced fluorescence and OH* chemiluminescence. *Combust. Flame* **2019**, *206*, 308−321.
(35) D'Anna, A. Combustion-formed nanoparticles. *Proc. Combust. Inst.* **2009**, *32*, 593−613.
(36) Bartos, D.; Dunn, M.; Sirignano, M.; D'Anna, A.; Masri, A. R. Tracking the evolution of soot particles and precursors in turbulent flames using laser-induced emission. *Proc. Combust. Inst.* **2017**, *36*, 1869−1876.
(37) Commodo, M.; De Falco, G.; Bruno, A.; Borriello, C.; Minutolo, P.; D'Anna, A. Physicochemical evolution of nascent soot

particles in a laminar premixed flame: From nucleation to early growth. *Combust. Flame* **2015**, *162*, 3854−3863.
(38) Minutolo, P.; D'Anna, A.; D'Alessio, A. On detection of nanoparticles below the sooting threshold. *Combust. Flame* **2008**, *152*, 287−292.
(39) Giusti, A.; Mastorakos, E. Turbulent Combustion Modelling and Experiments: Recent Trends and Developments. *Flow, Turbul. Combust.* **2019**, *103*, 847−869.
(40) Shih, T.; Liou, W.; Shabbir, A.; Yang, Z.; Zhu, J. A new k-ε eddy viscosity model for high Reynolds number turbulent flows. *Comput. Fluids* **1995**, *24*, 227−238.
(41) Miller, R. S.; Harstad, K.; Bellan, J. Evaluation of equilibrium and non-equilibrium evaporation models for many-droplet gas-liquid flow simulations. *Int. J. Multiphase Flow* **1998**, *24*, 1025−1055.
(42) Amsden, A. A.; Butler, T. D.; O'Rourke, P. J. *KIVA-II: A Computer Program for Chemically Reactive Flows with Sprays*; Los Alamos National Laboratory: Los Alamos, NM, 1989; LA-11560-MS, DOI: 10.2172/6228444.
(43) Jamali, S. Computational Modeling of Turbulent Ethanol Spray Flames in a Hot Diluted Coflow. Ph.D. Thesis, Delft University of Technology, Delft, Netherlands, 2014.
(44) Ma, L.; Roekaerts, D. Modeling of spray jet flame under MILD condition with non-adiabatic FGM and a new conditional droplet injection model. *Combust. Flame* **2016**, *165*, 402−423.
(45) Ihme, M.; See, Y. C. LES flamelet modeling of a three-stream MILD combustor: Analysis of flame sensitivity to scalar inflow conditions. *Proc. Combust. Inst.* **2011**, *33*, 1309−1317.
(46) Göktolga, M. U.; van Oijen, J. A.; de Goey, L. H. Modeling MILD combustion using a novel multistage FGM method. *Proc. Combust. Inst.* **2017**, *36*, 4269−4277.
(47) Lamouroux, J.; Ihme, M.; Fiorina, B.; Gicquel, O. Tabulated chemistry approach for diluted combustion regimes with internal recirculation and heat losses. *Combust. Flame* **2014**, *161*, 2120−2136.
(48) Sorrentino, G.; Ceriello, G.; de Joannon, M.; Sabia, P.; Ragucci, R.; van Oijen, J.; Cavaliere, A.; de Goey, L. P. H. Numerical Investigation of Moderate or Intense Low-Oxygen Dilution Combustion in a Cyclonic Burner Using a Flamelet-Generated Manifold Approach. *Energy Fuels* **2018**, *32*, 10242−10255.
(49) Nehse, M.; Warnat, J.; Chevalier, C. Kinetic modeling of the oxidation of large aliphatic hydrocarbons. *Symp. (Int.) Combust., [Proc.]* **1996**, *26*, 773−780.
(50) Giusti, A.; Mastorakos, E.; Hassa, C.; Heinze, J.; Magens, E.; Zedda, M. Investigation of Flame Structure and Soot Formation in a Single Sector Model Combustor Using Experiments and Numerical Simulations Based on the Large Eddy Simulation/Conditional Moment Closure Approach. *J. Eng. Gas Turbines Power* **2018**, *140*, 061506.
(51) Leung, K.; Lindstedt, R.; Jones, W. A simplified reaction mechanism for soot formation in nonpremixed flames. *Combust. Flame* **1991**, *87*, 289−305.
(52) Anand, M. S.; Eggels, R.; Staufer, M.; Zedda, M.; Zhu, J. An Advanced Unstructured-Grid Finite-Volume Design System for Gas Turbine Combustion Analysis. *Proceedings of the ASME 2013 Gas Turbine India Conference*; Bangalore, Karnataka, India, Dec 5−6, 2013; Paper GTINDIA2013-3537, DOI: 10.1115/GTINDIA2013-3537.

https://dx.doi.org/10.1021/acs.energyfuels.0c03860
Energy Fuels 2021, 35, 7092−7106